*V. M. Shevtsova*[1], *D. E. Melnikov, and J. C. Legros*

# The Study of Weak Oscillatory Flows in Space Experiments

*The effects of residual accelerations have been studied by using three-dimensional modeling of the flow in a rectangular cell filled with a liquid, Pr = 20, the walls of which were kept at different temperatures. The system was subjected to an acceleration field, which can be decomposed into two parts: a steady component and another one which varies slowly with time, the frequency is about* $f_0 \approx 10^{-3}$ *Hz. The convective heat transport and flow characteristics are discussed for different parameters of g-jitter. The high and low frequency modulation of a sinusoidal g-jitter is discussed. To capture many of the essential characteristics of buoyancy-induced convection a new approach is suggested, which was developed based on the observation of the trajectories of tracer particles. On the one hand, it is a typical way to record the flow in experiments. On the other hand, creating database of different types of trajectories gives the possibility to solve the inverse problem. The shape of the trajectory depends on the g-jitter parameters. It is shown that for slow convective motions the tracer particles perform loops along trajectory due to g-jitter with low frequencies, and the additional high frequencies only cause trembling of the shape of these loops. Taking the experimentally recorded trajectories of tracer particles and comparing with those in the database, one can draw a conclusion about the amplitude and direction of the resulting gravity vector during the experiment.*

## 1. Introduction

The understanding that residual acceleration can signifcantly affect the behaviour of fluids in low gravity experiments has led to some reviews [1-3], mainly concerning with space experiments on board of American vehicles. It is also expected that g-jitter vibrations will exist on the International Space Station (ISS) over a wide spectrum of frequencies. Some recent publications [4-5] have dealt with the estimation of the effect of g-jitter at future experiments on board the ISS.

The residual acceleration environment can cause convective flow rate, which is comparable to diffusive transport rate. Most of the previous studies to date have focused on the influence of vibrational accelerations on the crystal growth and related phenomena. For instance, Alexander [6] has shown that for sinusoidal oscillating accelerations, when the mean flow is negligible, a mean compositional non-uniformity will arise whenever the phase difference between the oscillating velocity and composition field is different from $\pi/2$.

For the last few decades the space experiments are increasingly aimed towards measuring different phenomena, especially thermo-physical properties of fluids. In these experiments any convective flow in the experimental cell is deleterious. Diffusion coefficient measurements are another excellent subject of microgravity utilization. The early space experiments have shown [7], that the diffusion coefficient can be measured in microgravity with several orders of magnitude more precision than is possible on Earth. However the accuracy of the measurements is still a delicate question. Matsumoto and Yoda [8] have numerically shown that low frequency g-jitter produces an error of about 8% in the accuracy of the diffusion coefficient measurements.

The residual accelerations, which are taken into account in the present study, correspond to the values of accelerations on a platform with an altitude around 200-400 km, which is rotating around its main axis. These values are typical for experiments on the sounding rockets and satellites, e.g. the Russian satellite Foton. Surely, it is almost impossible to exclude entirely gravity-induced convection, since there is always a residual gravity due to the atmospheric drag, the stabilizing rotation of the plat-

[1]Mail address: Dr. Valentina M. Shevtsova
MRC, CP-165/62, Université Libre de Bruxelles,
50, Av. F. D. Roosevelt, B-1050 Brussels, Belgium
Paper submitted: September 06, 2002
Submission of final revised version: May 22, 2003
Paper accepted: May 23, 2003

 

form and accelerations, which come from being off the centre of mass. The random acceleration due to spacecraft maneuvers is not considered here as scientific experiments on this type of vehicles have mainly been carried out in steady conditions. Although the residual acceleration provided by this vehicle is one of the best available up to now for long duration microgravity conditions, the induced convection is not necessarily negligible for some class of investigations, e.g. when the characteristic time is large as in diffussion controlled phenomena.

On the one hand the effect of low frequency g-jitters can be neglected for some fluid physics experiments. For example, on the Maser-8 a period of rotation was 6.9 minutes, for Foton-12 the period varied between 7-12 min. It leads to very low frequencies $f \approx 10^{-3}$ *Hz*. The amplitude of gravity varies from $3 \cdot 10^{-6}$ $g_0$ on Maser-8 and up to $10 \cdot 10^{-6}$ $g_0$ on Foton-12. On the other hand for weak flows this time-varying acceleration can change the trajectory of the experimental tracers, or affect the movements of gas inclusions (e.g. vapor bubbles in boiling phenomena). Usually, the processing of the experimental results is based on the knowledge of the trajectory of tracer particles. Also post flight analysis of some experimental data has shown that knowledge of gravity level is really important for a complete explanation of the physical phenomena [9].

The system was subjected to an acceleration field, which can be decomposed into two parts: a steady component and a fluctuating contribution (g-jitter). One of the aims of this paper is to evaluate accurately the intensity of the flow induced by the residual gravity. Some results of the numerical analysis are presented in a form of the trajectories of tracer particles. The shape of trajectories depends upon the parameters of g-jitter. This is a new approach to study the effect of g-jitter, which can allow the explanation of some space experimental results.

## 2. Mathematical formulation of the problem

In this study, the thermocapillary convection in a fluid that is enclosed in a laterally heated, threedimensional rectangular cell is investigated. Thermocapillary convection of an incompressible, Newtonian liquid with constant transport coeficients is considered. All the physical characteristics are taken constant, except the density which varies linearly with temperature in the buoyancy term, $\rho = \rho_0(1 - \beta\,(T - T_0))$ (Boussinesq approximation), where $\beta$ is the thermal expansion coefficient, and surface tension $\sigma(T)$ at the gas-liquid interface, which taken as a linear function of the temperature $\sigma = \sigma_0 - \gamma(T - T_0)$. The geometry of the cell is shown in fig. 1. It reflects real experimental situations when observation is done through the window, which occupies only one part of the cell. Two vertical isothermal sidewalls are kept at temperatures $T_h$ on the left and $T_c$ on the right, $T_h > T_c$. All other boundaries are assumed to be adiabatic.

Here we take into account the vector of the residual acceleration that has components in any spatial direction. The signs of $g_i$ are chosen in such a way that the direction of the component of

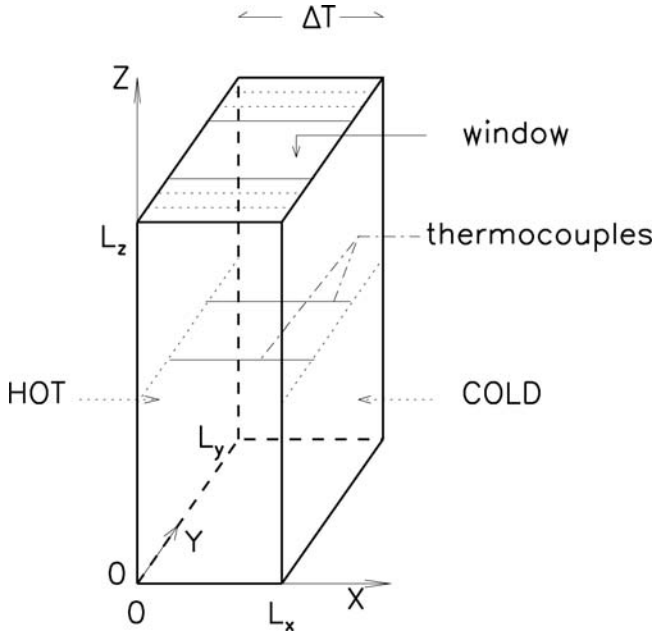


*Fig. 1. Geometry of the problem.*

residual gravity is opposite to the direction of axis of the coordinates. In the Cartesian coordinate system the 3-D non-dimensional Navier-Stokes, the energy, and the continuity equations are given by:

$$\frac{\partial U}{\partial t} + \Gamma_x U \frac{\partial U}{\partial x} + \Gamma_y V \frac{\partial U}{\partial y} + W \frac{\partial U}{\partial z} = -\Gamma_x \frac{\partial P}{\partial x} + \Delta U + Gr_x \left(\Theta - x + 1\right) \tag{1}$$

$$\frac{\partial V}{\partial t} + \Gamma_x U \frac{\partial V}{\partial x} + \Gamma_y V \frac{\partial V}{\partial y} + W \frac{\partial V}{\partial z} = -\Gamma_y \frac{\partial P}{\partial y} + \Delta V + Gr_y \left(\Theta - x + 1\right) \tag{2}$$

$$\frac{\partial W}{\partial t} + \Gamma_x U \frac{\partial W}{\partial r} + \Gamma_y V \frac{\partial U}{\partial y} + W \frac{\partial W}{\partial z} = -\frac{\partial P}{\partial z} + \Delta W + Gr_z \left(\Theta - x + 1\right) \tag{3}$$

$$\frac{\partial \Theta}{\partial t} + \Gamma_x U \left( \frac{\partial \Theta}{\partial x} - 1 \right) + \Gamma_y V \frac{\partial \Theta}{\partial y} + W \frac{\partial \Theta}{\partial z} = \frac{1}{\mathrm{Pr}} \Delta \Theta \tag{4}$$

$$\Gamma_x \frac{\partial U}{\partial x} + \Gamma_y \frac{\partial V}{\partial y} + \frac{\partial W}{\partial z} = 0 \tag{5}$$

where the Laplacian is

$$\Delta = \Gamma_x^2 \frac{\partial^2}{\partial x^2} + \Gamma_y^2 \frac{\partial^2}{\partial y^2} + \frac{\partial^2}{\partial z^2} \quad .$$

Equations (1)-(5) have to be solved together with the following boundary conditions:

- no-slip condition on the rigid walls:

$$\vec{V} = 0,$$

- constant temperature on hot and cold walls:

$$\Theta(x=0) = \Theta(x=1) = 0,$$

- thermal adiabatic conditions on the other walls:

$$\frac{\partial \Theta}{\partial \vec{n}} = 0.$$

Here the height of the cell $L_z$ is taken as the characteristic length for the reference velocity, time and pressure i.e.,

$$U_{ch} = \frac{\nu}{L_z}, \quad \tau_{ch} = \frac{L_z^2}{\nu}, \quad P_{ch} = \rho_0 U_{ch}^2 .$$

Let us note that $L_x$ - is the length of the cell in the direction of the temperature gradient, and $L_y$ - is the depth of the cell. Then introducing some characteristic values $x_{ch} = L_x$, $y_{ch} = L_y$, $z_{ch} = L_z$ two aspect ratios $\Gamma_x$ and $\Gamma_y$ appear in the system:

$$\Gamma_x = \frac{L_z}{L_x}, \quad \Gamma_y \frac{L_z}{L_y} \quad .$$

The dimensionless temperature is introduced as $\Theta_0 = (T - T_0)/\Delta T$, where $T_0 = T_c$. The linear temperature profile is subtracted from the total value $\Theta_0$ to have zero boundary conditions for the temperature in the direction of applied temperature gradient. Then, $\Theta = \Theta_0 - 1 + x$. The dimensionless parameters, which appear in the equations, are the Prandtl number and the Grashof number:

$$\mathrm{Pr} = \frac{\nu}{k}, \quad Gr_i^* = \frac{g_i \beta \Delta T L_z^3}{\nu^2} \quad .$$

This formal, "mathematical" choice of Grashof number, though convenient for carrying out the simulations, does not reflect the physical aspects of the problem. Indeed, the characteristic velocity of the flow generated by the thermocapillary stress is proportional to the horizontal component of the temperature gradient, $\Delta T/L_x$, rather than $\Delta T/L_z$. Therefore, similar to ref. [10], the physical phenomena are characterized by modified Grashof number (without superscript):

$$Gr_i = \frac{g_i \beta \Delta T L_x^3}{\nu^2} \left( \frac{L_z}{L_x} \right)^3 = \frac{Gr_i^*}{\Gamma_x^3} \quad . \qquad (6)$$

In the discussion of the experimental results the Rayleigh number ($Ra = Gr\ Pr$) is often used instead of $Gr$. Therefore on the plots the values of $Ra$ will be given. The numerical results presented below correspond to physical values of a mixture of Ethylene glycol and water. It is a typical mixture with viscosity around 2-3 cSt. The physical properties of this mixture are listed in Table 1. The data, which are given in Table 1, are extracted from the PhD thesis [11]. As it follows from the table, the viscosity of the liquid depends slightly upon the reference temperature. Taking into account the uncertainty

*Table 1. Physical properties of a mixture of Ethylene glycol and water.*

| $T_{ref}$ | ν | $\beta$ | $k$ | $\gamma = d\sigma/dT$ | $\rho$ |
|---|---|---|---|---|---|
| $K$ | $m^2/s$ | $1/K$ | $m^2/s$ | $N/mK$ | $kg/m^3$ |
| 283 | $2.836 \cdot 10^{-6}$ | $5.0 \cdot 10^{-4}$ | $(1.1 - 1.3) \cdot 10^{-7}$ | $-3.908 \cdot 10^{-4}$ | 1058.4 |
| 293 | $2.34 \cdot 10^{-6}$ | $5.03 \cdot 10^{-4}$ | $(1.1 - 1.3) \cdot 10^{-7}$ | $-3.908 \cdot 10^{-4}$ | 1053.1 |

in the definition of thermal diffusion, it appears that a realistic value for Prandtl number is around Pr = 20. This value will be used in all calculations.

The geometrical sizes of the considered cell are $L_x = 2 \cdot 10^{-2}$ $m$, $L_y = 5 \cdot 10^{-2}$ $m$, $L_z = 5 \cdot 10^{-2}$ $m$. It gives the following aspect ratios: $\Gamma_x = L_z/L_x = 2.5$, $\Gamma_y = L_z/L_y = 1$.

## 3. Numerical method and code validation

To solve the time-dependent Navier-Stokes, energy and continuity equations (1-5), written in a non-dimensional primitive-variable formulation in the Boussinesq approximation, a finite volume method is applied. A staggered mesh is used with scalar values, defined at the centers of the cells. The velocities are determined in the central nodes of the cell sides. Forward differences for time derivatives and central differences for spatial derivatives are used. An explicit scheme for all of the spatial derivatives in the equations is applied.

The computation of the velocity field at each time step is carried out with the projection method. The main idea of the method is that we may subdivide the initial momentum equation into two independent ones. At the first step a "provisional" velocity field $\vec{V}^*$corresponding to the correct vortex, but not satisfying the continuity equation (5), is computed neglecting the pressure gradient in the momentum equation:

$$\frac{\vec{V}^* - \vec{V}^n}{\Delta t} = -\nabla \left( \vec{V}^n \vec{V}^n \right) + \Delta \vec{V}^n + Gr \left( \Theta + z \right) \vec{e}_z \quad .$$

The equation defining the velocity field on the next time step includes only the pressure gradient term:

$$\frac{\vec{V}^{n+1} - \vec{V}^*}{\Delta t} = -\nabla p^{n+1} \quad . \qquad (7)$$

In order to calculate the pressure field the Poisson equation is computed:

$$\Delta p^{n+1} = \frac{1}{\Delta t} \nabla \vec{V}^* \quad . \qquad (8)$$

The boundary conditions for pressure are obtained by projecting the equation (6) on the outward normal unit $\vec{N}$ to the boundary $\partial$G.

$$\left( \frac{\partial p}{\partial N} \right)_{\partial G}^{n+1} = -\frac{1}{\Delta t} (\vec{V}_{\partial G}^{n+1} - \vec{V}_{\partial G}^*) \vec{N},$$

where $\vec{V}_{\partial G}^*$is the value of $\vec{V}^*$ on $\partial$G. If the boundary values for $\vec{V}^*$ and $\vec{V}^{n+1}$ are equal, the pressure gradient is zero. Thus, on the rigid walls the pressure derivatives in directions perpendicular to the wall are equal to zero:

$$\frac{\partial p}{\partial z} = \frac{\partial p}{\partial x} = \frac{\partial p}{\partial y} = 0 .$$

Finally, the velocity at the $(n + 1)$-time step is obtained from the requirement that $\vec{V}^{n+1}$ must be a divergence-free vector, i.e.

$$\vec{V}^{n+1} = \vec{V}^{*} - \Delta t \nabla p^{n+1} . \qquad (9)$$

The explicit ADI method is applied for solving the Poisson equation for pressure in the *x*, *y*-directions. To solve the Poisson equation in the *z*-direction, where all fields are uniform, the FFT (expansion only in cosine series) is used. The calculation of the buoyancy convection is validated by quantitative comparison with the well-known De Valh Davis test [12]. To make a comparison a 2-D stream function has been calculated from the 3-D results in the middle of the cell in *xz*-plane. One should expect lower values of the maximal velocities in the 3-D case, as the influence of front and backside walls and possible motion in the third direction are neglected in the 2-D case. Indeed, as it is written in Table 2, the maximal value of stream function, obtained from 3-D results, is about 4% less than the value for 2-D results. We consider this a favorable comparison as a proof of correctness of our code.

*Table 2. The values of $|\psi_{max}|$ Pr = 0.71, $\Gamma_x$ = 1, $\Gamma_y$ = 1.*

| | present work (3-D) | 2-D ref. [12] | 2-D Vahl Davis [13] bench mark solution |
|---|---|---|---|
| $Ra = 10^3$ | 1.584 | 1.654 | 1.653 |

## 4. Slowly varying in time perturbation of gravity field

In this part the study of the flow induced by superposed steady and slowly time varying weak accelerations is considered. This can result from the constant atmospheric drag coupled with the rotation of the platform. The frequency is known from post flight analysis of data [9, 13], it changes from $f \approx 1.4 \cdot 10^{-3}$ Hz to $f \approx 2.2 \cdot 10^{-3}$ Hz. But the direction and amplitude of g-jitter can be determined only through the response of velocity field. For the case when the vibration period ($\Pi$) is small compared to the characteristic time scales i.e., $\Pi << min(d^2/\nu, d^2/k)$ but still large enough to consider the fluid incompressible i.e., $\Pi >> d/c$ ($c$ is the speed of sound in the fluid) there is a well-developed averaging technique[15]. In the present situation, $\Pi = 600s$ and $\tau_v = d^2/\nu = 170s$, $\tau_k > 3000s$ this technique is not applicable, therefore the complete system of governing equations (1-5) will be solved with the constant amplitudes of the gravity vector $g_x^0, g_y^0$, the amplitude of g-jitter $g^{os}$ will be taken as a parameter. To evaluate the magnitude of the velocity of this flow the present 3-D calculations are done for the amplitudes of acceleration existing on Foton-12 during the ESA experiments in FluidPac. The amplitudes of accelerations are as following [9]:

$$g_x^0 = 3.81 \cdot 10^{-6} g_0, \; g_y^0 = 10 \cdot 10^{-6} g_0, \; g_z^0 = 0 . \qquad (10)$$

This section consists of 3 subsections: (1) the study of oscillatory flow and thermal characteristics; (2) the analysis of the trajectory of tracer particles which allow us to solve both direct and inverse problems for the fluctuating acceleration with non-zero mean value; (3) the study of some additional effects: differences in density between particles and liquid and the Coriolis force.

### *4. 1 Influence of g-jitter on the flow field and thermal characteristics*

For the parametric study the time-dependence in the gravity vector is considered as following:

$$\begin{aligned} g_x &= g_x^0 + g^{os} \sin \omega t, \\ g_y &= g_y^0 + g^{os} \cos \omega t, \\ g_z &= 0. \end{aligned} \qquad (11)$$

Here the dimensionless frequency $\omega = 2\pi\tau_v/\Pi = 11.19$ (the viscosity for the definition of $\tau_v$ is taken for the fluid at T = 293*K*) corresponds to $f = 1.67 \cdot 10^{-3}$ Hz. In the absence of g-jitter the maximum dimensionless velocity,

$$V_m = \sqrt{V_x^2 + V_y^2 + V_z^2} = V_m^0 = 8.65 \cdot 10^{-2}$$

for the above considered values, i.e.

$$g_x^0 = 3.8 \cdot 10^{-6} g_0 \text{ and } g_y^0 = 10 \cdot 10^{-6} g_0 .$$

When $g^{os} \neq 0$ the value of maximal velocity, $V_m$, oscillates with the frequency $\omega$ and the oscillations are in phase with the driving force in the direction perpendicular to the temperature gradient $V_m \sim \widetilde{V}_m \cos \omega t$ for the different combinations of constant and oscillatory components. The amplitude of velocity oscillations increases linearly with growth of $g^{os}$, see fig. 2(a). The fitting function $A_{vel} = k\, g^{os}$ is shown by dotted line, where $k = 1.74 \cdot 10^{-2}$. The oscillatory acceleration component of the driving force does not produce a mean flow. The time averaged velocity does not depend upon $g^{os}$ and equals the steady value $V_m = V_m^0 = 8.65 \cdot 10^{-2}$ .

Here the Nusselt number, which gives a measure of the *convective* heat transport in the x-direction through the hot or cold surface is defined as:

$$Nu_{conv} = \frac{q_{total} - q_{cond}}{q_{cond}} = \frac{q_{total}}{q_{cond}} - 1, \text{ where}$$

$$q_{cond} = -\int_s k \cdot \frac{\partial T}{\partial \vec{n}} dS = k L_y L_z \Delta T .$$

In the dimensionless variables it will take form

$$Nu_{conv} = -\int \frac{\partial \theta}{\partial x} dydz .$$

For the steady state conditions the convective fluxes on the cold and hot sides are equal i.e., $N_{ux=0} = N_{ux=1}$, when all other walls are thermally insulated. This condition is fulfilled in our numerical code with accuracy $10^{-7}$. For the static gravity, when $g^{os} = 0$

the convective heat transport is a constant value, $Nu = 0.353 \cdot 10^{-2}$.

With the additional oscillatory contribution in gravity vector, the Nusselt number begins to oscillate, and the time average convective heat transport sharply increases. With a further increasing of the amplitude of the oscillatory component the Nusselt number continues to grow but rather slowly. The time averaged Nusselt number for different amplitude of oscillation $g^{os}$ is given in fig. 2(b).

The time-dependent behavior of the Nusselt number is shown in fig. 3 for different combinations of the residual gravity. The accelerations are written directly on the plots. To demonstrate the jump of the Nu number with appearance of non-zero $g^{os}$, the solid horizontal line in fig. 3(a) corresponds to the case of static gravity. At the first case, fig. 3(a), the frequency of oscillations is the same, as the frequency of the driving force. However, there is a phase shift, different from $\pi/2$ when ($g_y^0 \neq 0$) between the temperature field i.e., the Nusselt number, and the driving force or velocity field,

$$Nu_{conc} = Nu_0 + A_{Nu} \cdot \sin(\omega t + \Delta\phi),$$

where $Nu_0$ is non-fluctuating contribution and $A_{Nu}$ is a constant. For example, for the set of parameters shown in fig. 3(a), $\Delta\phi = \phi_{Nu} - \phi_{vel} \approx 0.32\,\pi$. For the sinusoidally oscillating accelerations phase differences between the oscillating velocity and concentration fields have been previously observed by Alexander [6].

If the constant part of residual gravity in the dangerous direction is equal to zero, $g_y^0 = 0$ , e.g. eqs. (11) takes the form

$$\begin{aligned} g_x &= g_x^0 + g^{os} \sin \omega t\,, \\ g_y &= g^{os} \cos \omega t \end{aligned} \qquad (12)$$

the Nusselt number oscillates with a double frequency, see Figs. 3(b) and (c)

$$Nu_{conv} = Nu_0 + A'_{Nu} \cdot \sin 2\omega t$$

although the velocity and temperature field oscillates with frequency of the external signal $\omega$. A similar situation has been observed near the threshold of instability for the standing waves in liquid bridges [14].

It can be explained in the following way: the considered system is nonlinear. As the velocity is very small, e.g. term $V\nabla V$ in eq. (1-3) is negligibly small, the governing equations can be linearized. The response temperature to the external perturbation does not have pure sinusoidal form and contains a whole spectrum of harmonics $\Theta \sim \theta_m e^{\pm im\omega t}$. When the driving force has only a sinusoidal component the non-linear component of temperature field in $xy$-direction will be symmetrical, but with opposite sign. Look at the fig. 4(b), where isotherms deviate in the opposite directions from the linear profile at upper and lower parts. As the Nusselt number is an integral value, the input from the different components with main frequency drops down. The first super harmonics will result in the Nusselt number. As the amplitude of the first harmonic is much smaller than the amplitude of the main frequency, the amplitude of Nu oscillations is approximately 10 times smaller with respect to the previous case. Compare fig. 3(a) and fig. 3(b) with each other. The time average is not equal zero, as the non-linear interaction of two modes gives a contribution in non-oscillatory mode $m = 0$, although this particular value is very small $Nu_{conv} \approx 5 \cdot 10^{-4}$. For the same reason the time average Nu number increases with appearance of the oscillatory component in the gravity field, see fig. 2(b).

In the presence of oscillatory components in both directions, $g_x = g_x^0 + \tilde{g}_0 \sin \omega t$, $g_y = \tilde{g}_0 \cos \omega t$ the Nusselt number exhibits beating in amplitude, see fig. 3(c) (so-called modulation of amplitude). The difference in amplitude of two successive oscillations achieves maximum in the case of pure periodic oscillations in both directions $g_x^0 = 0$, $g_y^0 = 0$.

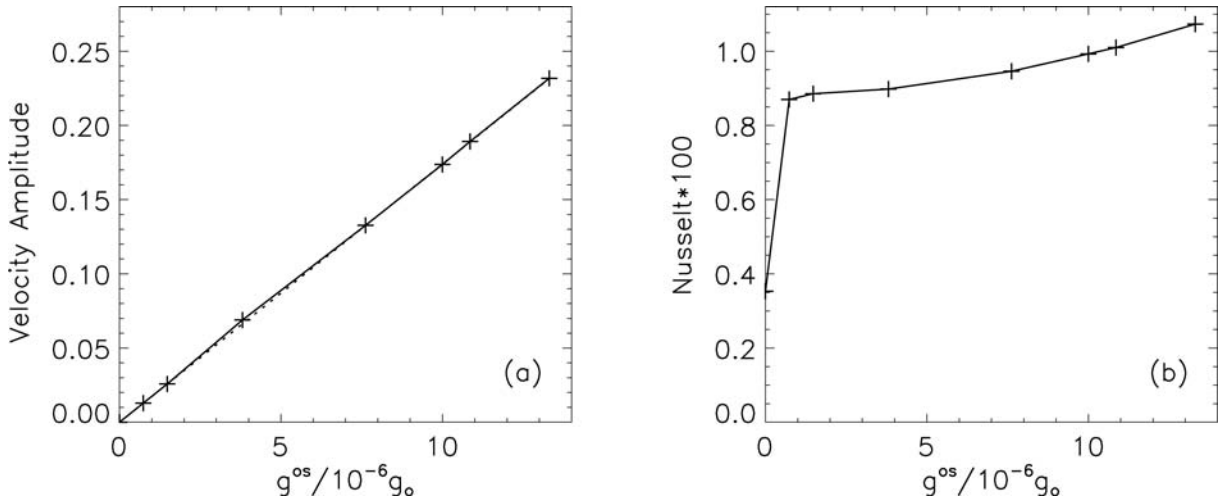


*Fig. 2. Dependence of (a) amplitude of maximal velocity and (b) time averaged Nusselt number upon the oscillating component of acceleration. The residual gravity is described by eq. (11).*

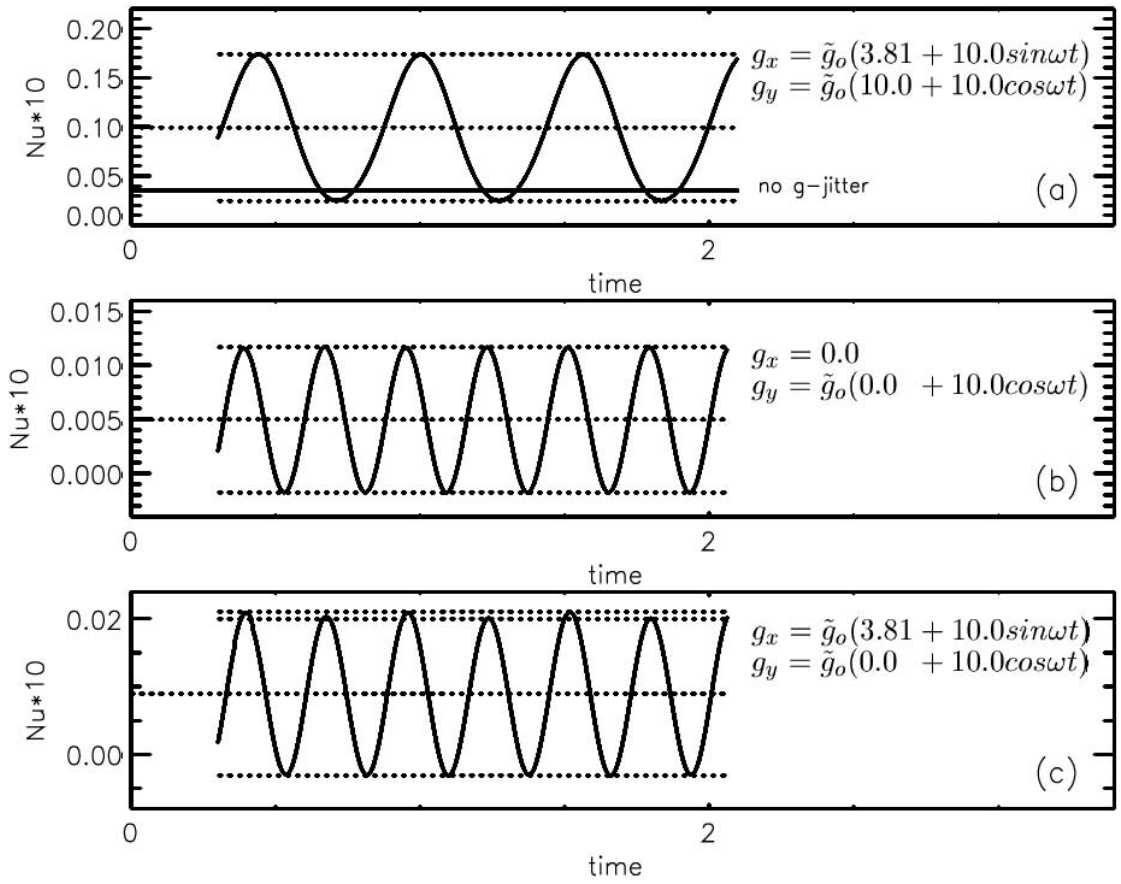


*Fig. 3. Time dependent Nusselt number for the different combinations of constant and oscillatory contributions of residual gravity. Here, $\tilde{g}_0 = 10^{-6} g_0$.*

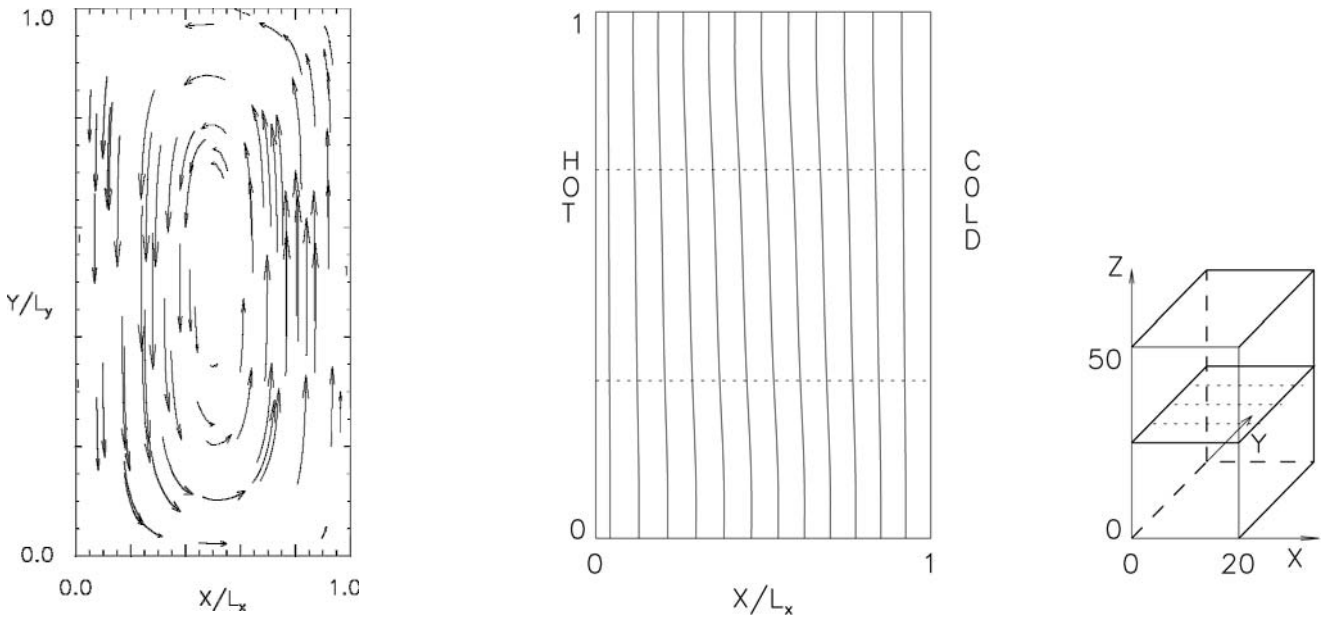


*Fig. 4. Velocity field (a) and temperature isolines (b) in horizontal XY-cross section for pure buoyant flow when $g_x^0 = 3.81 \cdot 10^{-6} g_0$, $g_y^0 = 10.0 \cdot 10^{-6} g_0$, $g^{os} = 0$, ($Ra_x = 32.97$, $Ra_y = 86.6$, $Ra_z = 0$, $\Delta T/\Delta x = 3$ K/mm).*

*4. 2 Influence of g-jitter on the trajectories of tracer perticles*

Usually, the processing of the experimental results is based on the knowledge of the trajectory of tracer particles. Due to residual gravity the tracer particles, iso-dense with liquid, move along the typical paths of convective flow, e.g. along the closed trajectories. The velocities of the flow have a maximum in the *xy*-plane, in perpendicular directions they are smaller by one or two orders of magnitude. Therefore one may infer that particles stay in the cross section *xy* when $z = 0.5$. Velocity field and temperature isolines at this cross section are shown in fig. 4 while the values of $g_x^0$, $g_y^0$ correspond to eq. (10) and $g^{os} = 0$.

The numerical trajectories of tracer particles have been reproduced in the *xy*-plane for the large spectrum of the acceleration amplitudes. In this section the tracer particles are assumed to have the same density as liquid. The dependence of the shape of the particle trajectory upon the value of g-jitter (oscillatory component $g^{os}$) is shown in fig. 5 for the same initial coordinates of particle during the same time interval. The crosses mark the position of the particle over equal time steps $\delta t$. With the appearance of the time-dependent contribution, the crosses on the trajectory are condensed in some places, indicating the local decreasing of the velocity due to existence of the oscillatory driving force. However, for $g^{os} < g_y^0$ the continues vortex flow is observed in the cell, although the trajectory becomes slightly distorted. When $g^{os}$ exceeds the value of $g_y^0$ due to the small inertia, the liquid follows circular motion and at some moment turns back and after a while continues motion in a primary direction. Some local return flows, so-called loops, are established, and they are clearly seen in fig. 5(c). The smaller loops exist in fig. 5(b), but they are not visible in the present scale. The excess of the oscillatory amplitude $g^{os}$ above $g_y^0$ is written directly on the plots, $\varepsilon = (g^{os} - g_y^0) / g_y^0$. The size of the loops in the direction of primary motion depends upon the value of the oscillato-

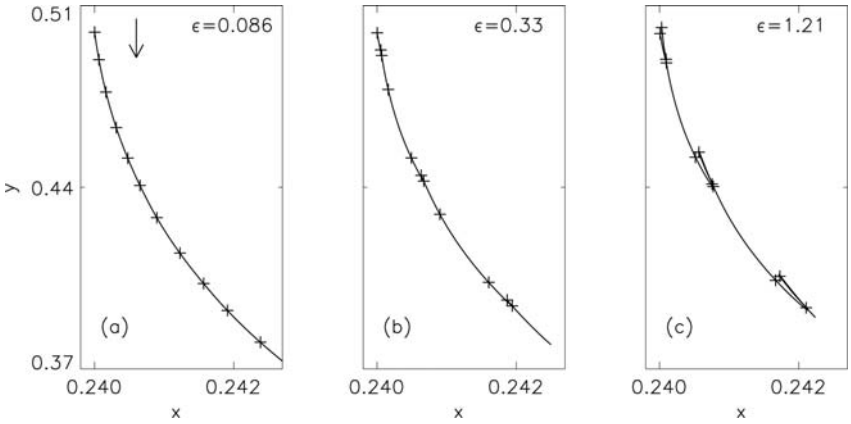


*Fig. 5. The dependence of the shape of the particle trajectory upon the value of g-jitter in the iso-dense liquid, see eq.(11). Here* $\varepsilon = (g^{os} - g_y^0) / g_y^0$. *Arrow shows the direction of the circular motion.*

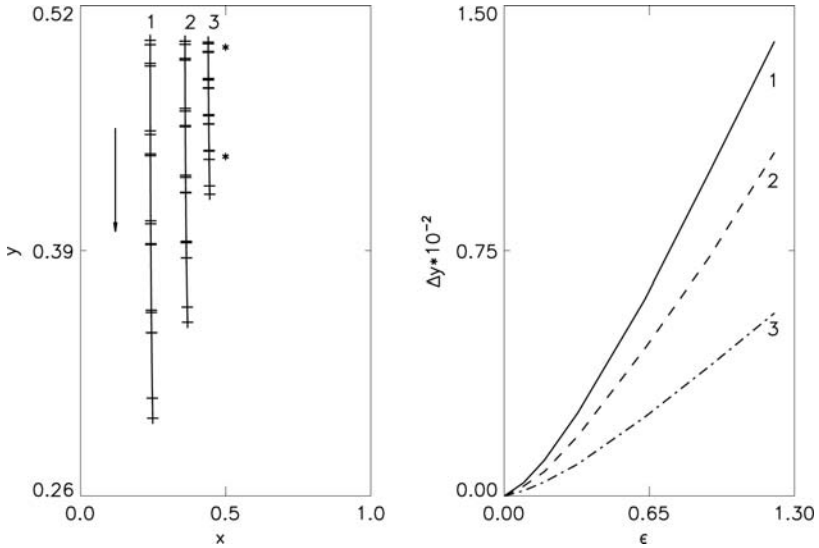


*Fig. 6. (a) The trajectory of iso-dense particles placed at the different distance from rigid walls,* $\varepsilon = 1.21$ *and (b) the dependence of the size of the loops performed by these particles upon value of g-jitter. The oscillatory component of the gravity vector exceeds the static component in dangerous direction,* $\varepsilon = (g^{os} - g_y^0) / g_y^0$.

ry component of the gravity field and upon location of the particle in the cell.

The trajectories of the particles, placed in three different positions in the cell, are shown in fig. 6(a) during 5 oscillation periods when $\varepsilon = 1.21$. The arrow indicates the direction of the flow. The loops are invisible on those scales, although the condensation of the crosses reveals them. During the time when the particle performs the loop, the "maximum" velocity changes the sign. These loops are very narrow and they are located very closely to the original path. These types of loops are difficult to detect in experiments. One may suggest that the scientist ought to be careful, when evaluating the velocity of the motion following the tracer particles. It is obvious that in the present case the velocity can be estimated incorrectly, as there are no "crosses" on the experimental trajectory.

The dependence of the size of the loops in the y-direction upon the value of g-jitter for these three particles is shown in fig. 6(b). As a general trend, the size of the loops strongly increases with a growth of $g^{os}$. However the particle, located in the stream with a higher velocity, performs a larger loops, see curve 1 in fig. 6(b). Those, located close to the center of the cell, perform smaller loops (curve 3 in fig. 6(b)). For the chosen particle the size of the loops along the trajectory practically remains constant in the central part of the cell. For example, for the third particle in fig. 6(a) the size of the first loop is only 3% larger than the size of the fourth loop. In fig. 6(a) stars indicate these loops. On a real scale the loops are not so tiny and can be easily determined by modern experimental equipments. The values of the size of the loops in *mm* are summarized in Table 3 for the wide spectrum of g-jitter values. For example, if $g^{os} = 2.21 \cdot 10^{-5} g_o$, $\varepsilon = 1.21$ the first particle performs loops whose size is 0.7 mm, and the size of the loop of the third particle, located closer to the center, is about 0.28 mm.

| $g_x^0 = 3.81 \cdot 10^{-6}\, g_0$, $g_y^0 = 10 \cdot 10^{-6}\, g_0$, $g_z^0 = 0$. | | | | |
|---|---|---|---|---|
| | | The size of the loops in mm | | |
| $g^{os}$ | ε | 1st particle | 2nd particle | 3rd particle |
| $10.86 \cdot 10^{-6}\, g_0$ | 0.086 | 0.020 | 0.015 | 0.008 |
| $11.82 \cdot 10^{-6}\, g_0$ | 0.18 | 0.055 | 0.037 | 0.022 |
| $13.30 \cdot 10^{-6}\, g_0$ | 0.33 | 0.128 | 0.094 | 0.049 |
| $16.26 \cdot 10^{-6}\, g_0$ | 0.63 | 0.301 | 0.226 | 0.121 |
| $19.21 \cdot 10^{-6}\, g_0$ | 0.92 | 0.496 | 0.385 | 0.199 |
| $22.17 \cdot 10^{-6}\, g_0$ | 1.22 | 0.695 | 0.525 | 0.280 |

*Table 3.: The size of the loops for different values of oscillatory component of residual gravity in mm.*

*4. 3 Role of some additional effects: viscous drag and Coriolis force*

The density of the particles $\rho_p$ has the same value as the liquid at particular temperature i.e. $\rho_l^0 = \rho_p^0$.

The estimations show that applying high temperature gradients like $\Delta T = 40 - 60\ K$ the difference of densities $\delta\rho = \rho_l - \rho_p$ becomes non-negligible. The Stokes velocity (free falling body) due to this $\delta\rho$ can be comparable with the velocity of the flow in the central part of the cell.

$$V = \frac{2}{9}\frac{r_0^2}{\eta}\left(\rho_l - \rho_p\right)\vec{g}_0 \approx \frac{2}{9}\frac{r_0^2}{\nu\rho_p^0}\frac{d\rho_l}{dT}\Delta T\,\vec{g}_0,$$

$$\rho_l = \rho_l^0 + \frac{d\rho_l}{dT}\Delta T.$$

For the properties of the liquid and particles, listed in Table 1, the velocity of viscous drag is equal

$$V = 2.852 \cdot 10^3\ r_o^2\,\vec{g}_o.$$

For the considered values of static residual gravity the maximal velocity of large particles (diameter 1mm) can achieve $V_x^{max} \approx 2.67 \cdot 10^{-8}$ *m/s* and $V_y^{max} \approx 6.9 \cdot 10^{-8}$ *m/s* ($V_{ch} = 0.468 \cdot 10^{-4}$ *m/s*.) The component of Stokes velocity in the y-direction is much

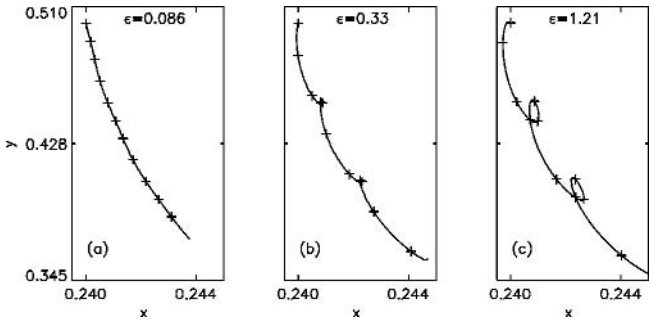


*Figure 7: The dependence of the shape of the trajectory for non iso-dense particles upon the value g-jitter. Here $g_x^0 = 3.81 \cdot 10^{-6} g_o$, $g_y^0 = 10.0 \cdot 10^{-6} g^o$ and $\varepsilon = (g^{os} - g_y^0)/g_y^0$.*

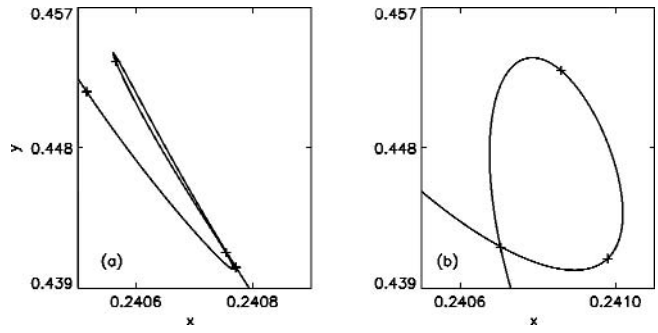


*Figure 8: The shape of the trajectory for (a) iso-dense and (b) non iso-dense particles, $\varepsilon = 1.21$.*

smaller, than those for the convective flow without g-jitter. But the component of the velocity in the x-direction, in the middle of the XY-plane is even large than those for convective flow. For example, for the first particle in fig. 6(a) the X-component of the convective velocity is about $1.79 \cdot 10^{-8} m/s$. From first appearance this difference is not very important, but it produces a large impact on the trajectory of the tracer particles. The trajectories of the particles whose density is different from the liquid are shown in fig. 7 for the same values of the oscillatory gravity component as in fig. 5. Due to the viscous drag the trajectory itself become more undulatory and the loops are essentially wider in the X-direction. This type of return flow can be described as a "lasso" like loop. Although the sizes of the loops in fig. 5 are very distinct for different $\varepsilon$ they are performed during the same time interval: three crosses on the loop. This can be explained by the fact that oscillatory component of acceleration does not produce a mean flow. The shape of the loops for iso-dense and non iso-dense particles is compared in fig. 8 through the microscopic scale. Both cases, fig. 8(a) and fig. 8(b), correspond to the same $g^{os} = 22.17 \cdot 10^{-6}\, g^0$, $\varepsilon = 1.21$. Again, the loops are performed within the same time interval (three crosses on the loop) and the dimension of the loops in y-direction is approximately the same. Only the flat shape of the loop in x-direction for iso-dense case changes to the circular one in the non iso-dense case. The trajectories will be completely different in the absence of constant residual gravity in the direction, perpendicular to the temperature gradient, that is when $g_y^0 = 0$, as the fluctuating acceleration field has zero mean. If there is only an oscillatory component in the dangerous direction $g_x = 0$, $g_y = g^{os} \cos\omega t$, $g_z = 0$ the liquid executes pure oscillatory movement. When there are two pure oscillatory components,

$$g_x = g^{os} \sin\omega t,\ g_y = g^{os} \cos\omega t,\ g_z = 0$$

the particle trajectory is slightly shifting along the x-axes, see fig. 9(a). But this shift is so tiny, that it is possible to recognize

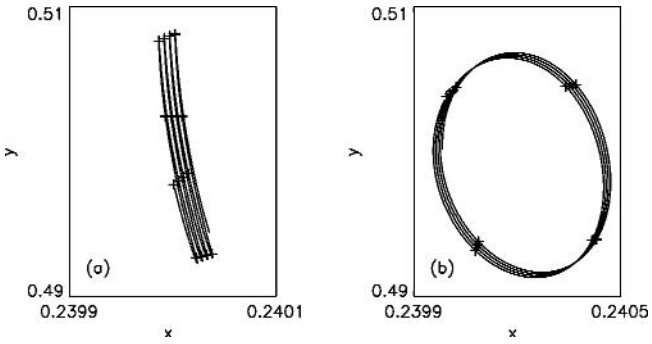


*Figure 9: The shape of the trajectory of the particle in the absence of static component in dangerous direction. $g_x = 0$, $g_y = 10.0 \cdot 10^{-6} g^0 \cos\omega t$; (a) Densities of liquid and particle are equal. (b) Densities of liquid and particle are different.*

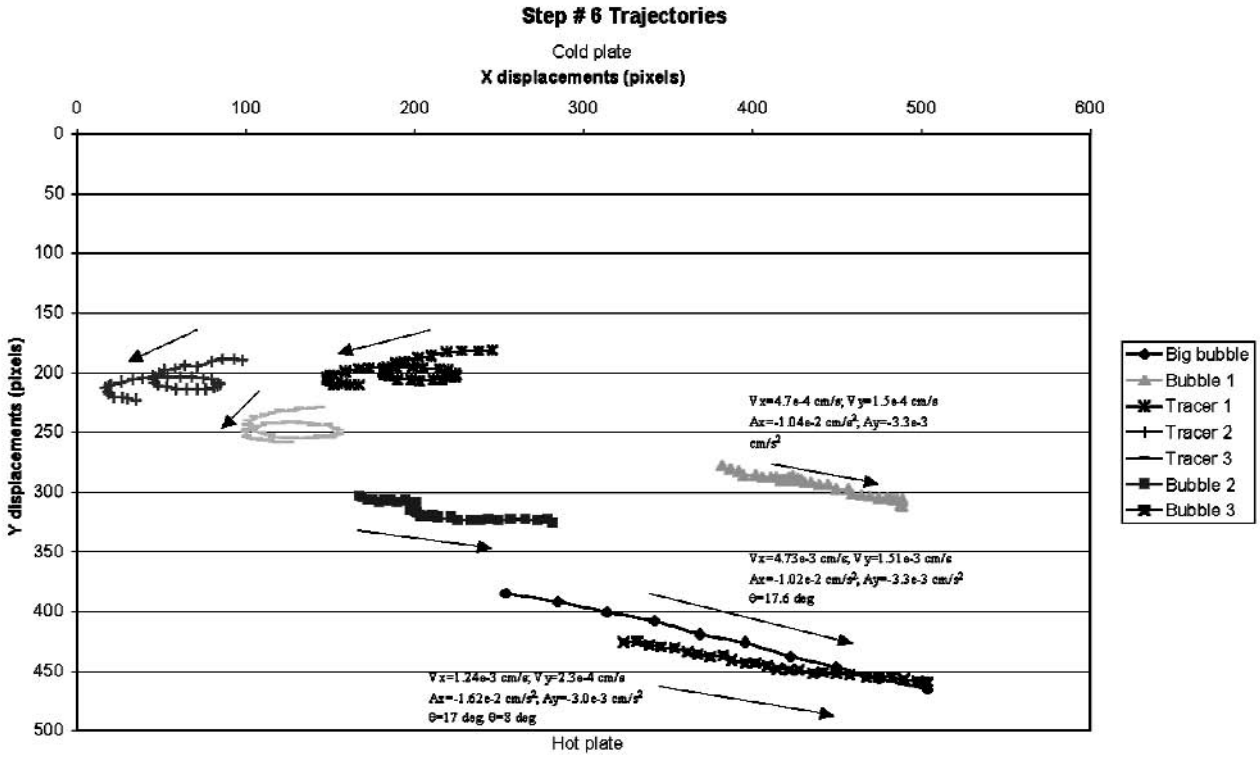


*Figure 10: The trajectories of tracer particle motion due to residual gravity observed during space experiment in ref. 16. (Courtesy the authors)*

it only through a microscope, e.g. the scale in x-direction is strongly stretched. In the presence of viscous drag (non iso-dense case) the particle follows a closed loop, see fig. 9(b). The shape of the loop depends upon the ratio of convective and Stokes velocities: it can vary from an ellipse to the perfect circle. Comparing the experimental trajectories with those, on fig. 5, fig. 7 and fig. 9, one can draw a conclusion about the relative ratio of different components of residual gravity in the real space experiment of interest. A few numerical runs have been made taking the Coriolis force into account. The analysis of the numerical results shows that the Coriolis force in combination with a buoyancy force does not change the structure of the flow, and the maximal values of velocities are increased by one tenth of percent. In the absence of g-jitter the maximum dimensionless velocity, $V_m^0$ is increased from $8.65 \cdot 10^{-2}$ to the value $8.66 \cdot 10^{-2}$ in the case with the Coriolis force. So, for the problem on hand, the Coriolis force could be neglected as a counterpart of buoyancy flow. Creating a database of different types of trajectories gives us the possibility to solve the inverse problem. This is particularly important, as it is not always possible to extract from post-flight data the precise value of the amplitude of 3-D time-dependent gravity vector. The experimental results from ref. [16], reproduced in fig. 10 have been given to us by courtesy of their authors. Due to the physical phenomena it is expected that tracer particles will move from hot to cold plate. But the residual gravity has masked this motion. In fact the different types of loops have been followed by tracer particles. With our current experience, and looking at these experimental results one can draw the conclusions that: a) the residual gravity had steady and fluctuating components; b) the steady amplitude is smaller than the amplitude of the oscillating contribution; c) for the working temperature difference the density of particles is different from the density of the liquids.

## 5 Perturbations of the sinusoidal profile of g-jitter

*5.1 Variations of the oscillation frequency*

The analysis, described above, dealt with a constant frequency of g-jitter, i.e. $\omega_0 = 11.19$, which corresponds to the period of a rotation 10 *min.* Eventually the frequency of the rotation of a satellite grows rather rapidly during the first days of the flight and keeps a constant small growth rate later during the mission if no stabilization action takes place, see ref. [9]. The influence of the variation of the fundamental frequency on the flow pattern is discussed here. The dependency of the gravity vector upon frequency is defined by eq.11. Closely related to the experimental conditions two different frequencies are considered: below and above the fundamental one, $\omega = 15.99$ and $\omega = 9.33$, which correspond to the period of the rotation 7 *min* and 12 *min* respectively. The trajectories of the tracer particles in the experimental fluid cell are modified by the frequencies of g-jitter, see fig. 11. On each curve in fig. 11 the time intervals between 2 crosses are the same. With the increasing of the oscillation frequency the size of the loops steps down and the particles loop more frequently along the vortex line. This is clearly visible from the comparison of different plots in fig. 11. Analyzing the sizes of various loops for the different frequencies it is found that the value

$$l \cdot \omega = const$$

is invariant for a defined location in the cell; here $l$ is the length of the loop.

*5.2 Low frequency modulation of the sinusoidal g-jitter*

Carrying out microgravity experiments with long characteristic time scale, e.g. during diffusion driven phenomena, one should take into account even smaller frequencies, than described above. A satellite, moving around the Earth, performs one turn during ≈90 *min.* This motion will cause the modulation of the periodical g-jitter, determined by eq.11. To demonstrate the role of this orbital motion with very low frequency, $f \approx 10^{-4}$ *Hz*, numerical modeling has been done for the following profile of micro acceleration

$$g_x = g_x^0 + g^{os}(1 + sin\Omega t)\, sin\, \omega 0t,$$

$$g_y = g_y^0 + g^{os}(1 + sin\Omega t)\, cos\omega 0t, \qquad (14)$$

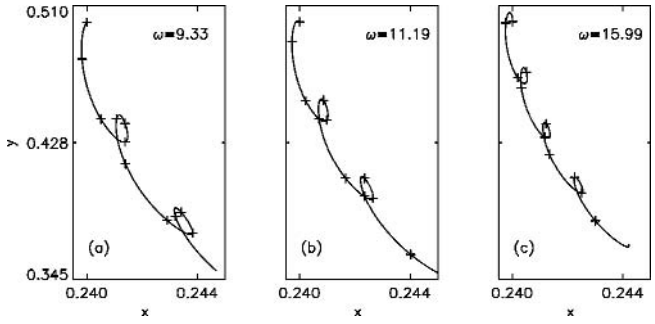


*Figure 11: The dependence of the shape of the trajectory for non iso-dense particles upon the frequency of g-jitter. Here $g_x^0 = 3.81 \cdot 10^{-6}\, g_0$, $g_y^0 = 10.0 \cdot 10^{-6}\, g_o$ and $\varepsilon = (g^{os} - g_y^0) / g_y^0 = 1.21$.*

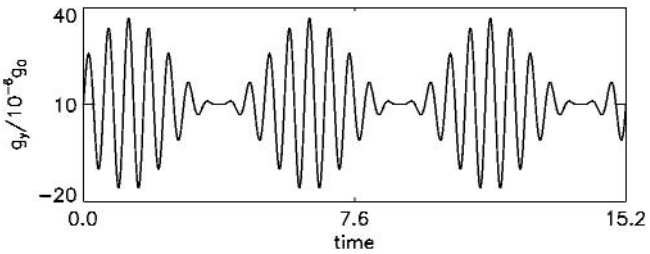


*Figure 12: Low frequency perturbations of the sinusoidal micro acceleration profile; the resulting time-dependent signal in the direction, perpendicular to the temperature gradient, $g_y$, see eq. 14. Here $g_x^0 = 3.81 \cdot 10^{-6}\, g_0$, $g_y^0 = 10.0 \cdot 10^{-6}\, g_o$ and $\varepsilon = 0.33$.*

$$g_z = 0.$$

where $\Omega = \omega_0/9$. This ratio between the frequencies corresponds to satellite Foton-12, own in 1999 with ESA experiments on-board, see ref. [9]. To emphasize the effect, the amplitudes corresponding to both frequencies are chosen being equal. Therefore the basic sinusoidal signal is strongly modulated, see fig. 12. It is expected that for actual experiments the modulation could be smaller. The displacement of non iso-dense tracer particle in x- and y-directions with time is shown in fig. 13. Due to the modulation of the sinusoidal signal of g-jitter, a wavy part of the trajectory of the tracer particles is followed by a smooth part. When the particle is mainly moving in one direction, either x- or y-direction ($\partial_t x \to 0$, $\partial_t y \to 0$), the wavy paths in x- and y-directions are out of phase. Out of phase means that one of the coordinates oscillates, while another is plane. For example, the amplitude of the oscillations of y-coordinate has a local maxima, when x-coordinate is smooth and almost constant, e.g. $x \approx 0.75$ and $x \approx 0.25$, in fig. 13. This takes place when the particle is moving along the sidewalls. On the other side, when the particle is turning near the corners of the cell, following the vortex line, both coordinates oscillate simultaneously. In fig. 13 this is happening between the vertical lines for the time interval $4 < t < 7$. The particle trajectory in (x,y) representation for the intervals designated as a, b, and c is shown in fig. 14. The Figs. 14(a), (b), (c) illustrate the trajectory for the same a, b, c time intervals. The sizes of the loops depend upon the amplitude of the micro acceleration level, given by eq.14 and shown in fig. 12. When the amplitude tends to zero, there are no loops on the trajectory, see fig. 14(a). With the growth of the amplitude the trajectory is bended and at the next step the loop is performed, see fig. 14(b). For this type of dependency g(t) each loop has various size, see fig. 14(c). One may note that the sizes of the loops are modulated with the frequency $\Omega = \omega_0/9$.

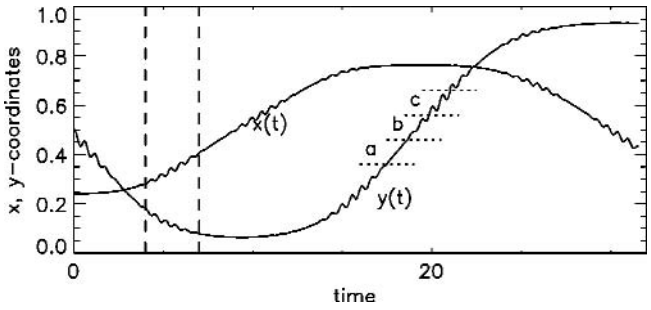


*Figure 13: The displacement of a non iso-dense tracer particle in x- and y-directions with time caused by the micro acceleration profile, shown in fig. 12. The particle trajectory in coordinates (x,y) for the intervals designated as a, b, c is shown in fig. 14*

*5.3 High frequency modulation of the sinusoidal g-jitter*

On-board a satellite, except the drifting frequency of a vehicle rotation, the periodical profile of the micro acceleration in the experimental cell can be modified by some external forces. One of the obvious sources of high frequency disturbances is a trembling of the body of spacecraft and operation of on-board payloads. To model numerically this additional type of high frequency disturbances to the periodical gravity field, the components of the gravity vector are defined by eq.14 but the frequency is chosen as $\Omega = 9\omega_0$. The time dependent behavior of one of the components of the gravity field, $g_y$, defined by eq.14 is shown in fig. 15(b). The loops shown in fig. 7(b) and fig. 15(b) correspond to the same set of parameters and they are given in the similar scale. Basically, only the tremulous shape of the loops manifests the role of high frequency oscillations. With increasing of the frequency $\Omega$ the trembling of the shape will be observed on the smaller scale.

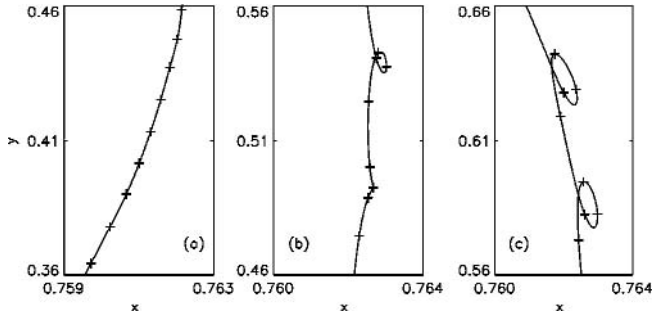


*Figure 14: The trajectory of the tracer particle when the periodical g-jitter is modulated by the low frequency perturbations. The plots a, b, c correspond to the displacement of the particle at the successive time intervals, shown in fig. 13. Here $g_x^0 = 3.81 \cdot 10^{-6} g_0$, $g_y^0 = 10.0 \cdot 10^{-6} g_o$ and $\varepsilon = 0.33$.*

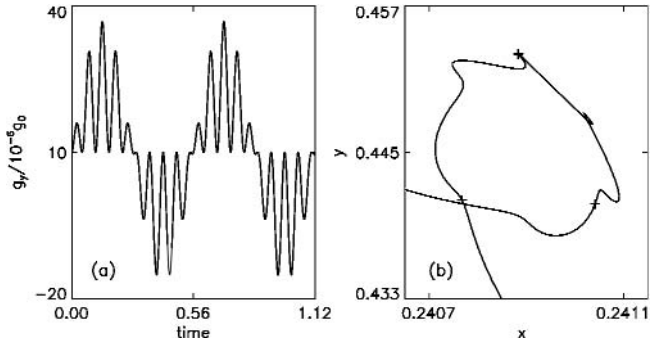


*Figure 15: High frequency perturbations of the periodical micro acceleration profile, see eq.14 where $\Omega = 9\ \omega_0$; (a) the resulting time-dependent signal in the direction, perpendicular to the temperature gradient, $g_y$ and (b) the shape of the trajectory of the tracer particles due to this acceleration field.*

## 6. Conclusions

The effects of residual accelerations on the behavior of a liquid have been studied using threedimensional modeling in a rectangular cavity with differentially heated walls. The amplitudes of steady and fluctuating accelerations have been chosen close to those measured on the Russian satellite Foton. However, the majority of the results obtained are very general and applicable to all types of low frequency g-jitters. These conclusions below are presented in such a way, they are interesting from a theoretical point of view and useful for the experimenters. The system is subjected to an acceleration field, which can be decomposed into two parts: a steady component and a time-dependent contribution. The consequent flow in the rectangular cell with aspect ratios, $\Gamma_x = 2.5$, $\Gamma_y = 1$, filled by liquid with Prandtl number, Pr = 20, was investigated. The results of the 3-D simulations show that taking into account only component of the acceleration, which is constant in time, the velocity of the flow induced by buoyancy force is rather small. Depending upon the applied temperature differences $\Delta T$ = 10 - 60*K*, the values of the maximal velocity vary in the range 0.6 - 4.05 $\cdot$ $10^{-6}$ *m/s*. In the case of slowly varying acceleration with non-zero mean, $f_0$ = 1.67 $\cdot$ $10^{-3}$, the resulting velocity and Nusselt number oscillate with the frequency of the driving force. The amplitude of velocity oscillations increases linearly with the growth of the amplitude of the fluctuating component of gravity, but this contribution does not produce mean flow. Contrary to this, the time average convective heat transport, e.g. Nu, grows with the appearance of a time-dependent component. In the case when the time average acceleration is equal to zero, the Nusselt number oscillates with a double frequency of the external signal $2f_0$. This is the result of second order effects, when input from the different components with the main frequency drops down.

Usually, the processing of the experimental results is based on the knowledge of the trajectory of tracer particles. Somehow in the numerical studies this approach has been missed. We have found that presentation of numerical results in the form of trajectory of tracer particles can give important information about the type of the residual acceleration and properties of the particles. The shape of trajectories depends upon the characteristics of the g-jitter. Due to steady residual gravity the tracer particles of the same density as the liquid, move along the typical paths of convective flow, e.g. along closed circular trajectories. With the appearance of the time-dependent contribution the shape of the trajectory becomes slightly distorted, although the continuous vortex flow is observed in the cell. When the amplitude of the fluctuating contribution $g^{os}$ exceeds the value of the residual gravity in dangerous direction, $g_y^0$, the liquid follows circular motion and at some moment turns back and after a while continues motion in a primary direction. Some local return flows, so-called loops, are established. These loops are very narrow and they are located very close to the original path. Therefore this type of loops is difficult to see in experiments, but they bring an error to the estimation of the velocity of the flow. The size of the loop in the direction of primary motion growth with the increase of $\varepsilon = (g^{os} - g_y^0)/g_y^0$ . In the case of acceleration varying in time with zero mean, the particles perform a cosine motion. Little additional drift occurs in the x-direction, if the gravity component in this direction is non-zero, $g_x \neq 0$. If the density of the particle is different from the density of the liquid, the local return flow takes a shape of lasso-like loops. Modern experimental rigs can detect them. In the case of varying in time acceleration with zero mean, particles perform a local circular motion. Depending upon the physical properties and location of the particle it can be a perfect circle or an ellipse. It is obtained that the variations of the oscillation frequency lead to modifications of the shapes of loops along the trajectory. The low frequency modulation $\Omega = \omega_0/9$ of periodical sinusoidal g-jitter causes the modulation of the size of the loops. The high frequency modulation $\Omega = 9\,\omega_0$ results in the tremulous shape of the loop. The present study emphasizes that the lower frequencies, e.g. $f \approx 10^{-3}$ Hz, existing simultaneously with a higher ones, can play the most important role for the diffusion driven phenomena in space. Creating a database of different types of trajectories gives us the possibility to solve the inverse problem. This is particularly important, as it is not always possible to extract from post-flight data the precise value of the amplitude of 3-D time-dependent gravity vector. For example, with our current experience the type of the residual gravity present during the space experiment in ref.[16] can be identified. Also the relative ratio of the amplitudes of the constant and of the oscillatory parts of the acceleration vector can be determined.

## Acknowledgments

This paper presents research results of the Belgian program on Interuniversity Pole of Attraction initiated by the Belgian state, Prime Minister's Office, Science Policy Programming (PAI 04-6). The scientific responsibility is assumed by the authors. The authors wish to thank Prof. Ranga Narayanan for helpful discussion.

## References

[1.] *Ostrach, S.:* Convection phenomena of importance for materials processing in space. Cospar Symposium on Materials Sciences in Space, Philadelhia, PA., June 9-10, (1976).

[2.] *Dressler, R. F.:* Transient thermal convection during orbital space flight. J. Cryst. Growth, vol. 54, p. 523 (1981).

[3.] *Alexander, J. I. D.:* Low gravity experiment sensitivity to residual accelerations. A review. Microgravity Sci. Technol., vol. 3, p. 52 (1990).

[4.] *Hurle, D. T.(ed.):* Proceedings of the Physical Sciences Working group Workshop on g-sensitivity of planned experimentation on the International Space Station. ESTEC, Noordwijk, The Netherlands, 10-11 September, 1998, Microgravity Sci. Technol., vol. 11, 2/3 (1998).

[5.] *Monti, R., Savino, R., Lappa, M.:* On the convective disturbances induced

by g-jitter on the Space Station. 51st IAF Congress, 2-6 October 2000, Rio de Janeiro (Brasil), IAF-J.2.03 (2000).

[6.] *Alexander, J. I. D.:* Residual gravity jitter effects on fluid processes. Microgravity Sci. Technol., vol. 7, p. 131 (1994).

[7.] *Frohberg, fig., Kraatz, K.-H., Wever, H.:* 5th European Symposium on Material Science under Microgravity-Results of Spacelab-1. ESA-SP-222, p. 201 (1984).

[8.] *Matsumoto, S., Yoda, S.:* Numerical study of diffusion coeffcient measurements with sinusoidal varying accelerations. Journal of Applied Physics, vol. 85, p. 8131 (1999).

[9.] *Shevtsova, V. M., Melnikov, D.E., Legros, J.C.:* The Post Flight Study of Microgravity Acceleration On-Board of Russian Spacecraft Foton-12. ESA Report, 135 p. (ESTEC, Noordwijk, The Netherlands, January, 2002).

[10.] *Shevtsova, V. M., Nepomnyashchy A.A., Legros J.C.:* Thermocapillary-buoyancy convection in shallow cavity heated from the side. Physical Review E., **67,** 066308, (2003).

[11.] *Bryan Clair Hoke, jr.:* Breakdown Phenomena of Evaporating Liquid Film Mixtures. Ph.D. thesis (1992).

[12.] *De Vahl Davis, fig.:* Natural convection of air in a square cavity: a bench mark numerical solution. Int. J. Numer. Meth. Fluids, vol. 3, p. 249 (1983).

[13.] *Shevtsova, V. M., Melnikov, D.E., Legros, J.C.:* Non-desirable convective motion on board space vehicles. Proceedings of the Foton/Bion International Conference, Samara, Russia, 25-30 June 2000, p. 101 (2000).

[14.] *Leypoldt, J., Kuhlmann, H. C., Rath, H.J.:* Three-dimensional numerical simulations of thermocapillary flows in cylindrical liquid bridges. J. Fluid Mech., vol. 414, p. 285 (2000).

[15.] *Gershuni, G. Z., Lubimov, D.V.:* Thermal vibrational convection. John Wiley &Sons, (1998).

[16.] *Albanese, C., Peluso, F., Castagnolo, D.:* Thermal radiation forces in microgravity, the TRUE and TRAMP experiments: results and future perspectives. Proceedings of the 1st International Symp. on Microgravity Research & Applications in Phys. Sci.&Biotechnology, Sorrento, Italy, 10-15 September 2000 (ESA SP-454, January 2001), p. 755 (2001).